Simulating the Palmer-Chalker state in an orbital superfluid

Hua Chen *

Department of Physics, Zhejiang Normal University, Jinhua 321004, China

(Received 14 November 2019; accepted 14 May 2020; published 1 June 2020)

We consider a bosonic *s*- and *p*-orbital system in a face-centered-cubic (fcc) optical lattice and predict a fluctuation-induced instability towards the orbital analog of the Palmer-Chalker state, which was originally proposed in an electronic spin system. For bosons loaded in the fcc optical lattice, the single-particle spectrum has four degenerate band minima with their crystal momenta forming a tetrahedron in the Brillouin zone. In the weakly interacting regime, the ensuing many-particle ground state, at the classical level, underlies a four-sublattice tetrahedral supercell of spontaneously generated *p*-orbital angular momenta through the Bravais-Bloch duality between real and momentum space and is macroscopically degenerate, originating from the geometric frustration. The fluctuations on top of the classical ground state lift its degeneracy and select the Palmer-Chalker ordering of *p*-orbital angular momenta as the quantum ground state through an order-by-disorder mechanism. These findings raise the exciting possibility of simulating the Palmer-Chalker state with its orbital counterpart in ultracold atomic gases.

DOI: 10.1103/PhysRevA.101.063601

I. INTRODUCTION

Geometric frustration, usually characterized by a macroscopic degeneracy of the classical ground-state manifold, is a key attribute of emerging exotic quantum ground states. Such a degeneracy in the energy landscape arises from competing interactions and can be lifted by quantum fluctuations or additional interactions, thereby selecting a unique ground state. A pertinent issue of relevance is the quantum magnets on geometrically frustrated lattices [1]. For example, the classical ground state of the Heisenberg antiferromagnet on a pyrochlore lattice composed of frustrated corner-sharing tetrahedra has a macroscopic degeneracy [2,3]. The dipolar interaction, which serves as the perturbation to the isotropic Heisenberg exchange, lifts the classical degeneracy and selects the unique magnetic state, called the Palmer-Chalker (PC) state [4]. In recent decades, intensive experimental effort has been devoted to the search for this state in pyrochlore oxides [5,6]. To date, the inelastic neutron scattering measurements show compelling evidence of the PC state in several compounds including $Gd_2Sn_2O_7$, $Er_2Sn_2O_7$, and $Er_2Pt_2O_7$ [7–10]. The microscopic origin of the observed PC state, however, has remained enigmatic for the diverse interactions arising in its proximity to competing phases.

Ultracold atomic gases, on the other hand, have natural advantages in the quantum simulation of artificial solids in optical lattices [11,12]. In particular, recent experiments have observed orbital superfluidity in two-dimensional bipartite optical lattices with the sublattices accommodating *s* and *p* orbitals [13–17]. It is crucial that the coherence between *p* orbitals established by the tunneling process via *s* orbitals leads to an unexpectedly long lifetime of atoms in high Bloch bands. Theoretically, these experimental settings have also inspired numerous theoretical proposals to simulate the interacting orbital physics in optical lattices [18–25].

Here we propose a concrete protocol to realize the PC state with nontrivial interplay between the lattice geometry and orbital anisotropy. It is worth remarking that the nature of the PC state studied in the electronic spin systems is a Mott insulator, in which the electronic charge degree of freedom is frozen by strong correlations. In contrast, the PC state we propose can be induced by the fluctuations from local Hubbard interactions in a weakly interacting Bose gas. Specifically, we generalize the *sp* orbital system from a two-dimensional bipartite lattice to a three-dimensional face-centered-cubic (fcc) lattice by retaining the essential bipartite ingredient. A remarkable feature is that the band structure has four degenerate energetic minima with the crystal momenta forming a tetrahedron in the Brillouin zone. This yields a finite-momentum condensate for weakly interacting bosons. Within the Gross-Pitaevskii approximation, the multiorbital Hubbard interaction breaks time-reversal symmetry with spontaneous *p*-orbital angular momenta residing on a geometrically frustrated tetrahedral superlattice. The classical ground state thus has extensive degeneracy due to the emergent frustration, which prevents the system from choosing a unique ground state. The fluctuations described by the standard Bogoliubov theory are further examined in the ground-state selection. Finally, we show that the PC ordering of *p*-orbital angular momenta is favored by quantum and thermal fluctuations via the order-by-disorder mechanism [26–29]. The predicted PC state in the superfluid phase is characterized by three linearly dispersing Nambu-Goldstone (NG) modes [30,31] with one arising from the broken global U(1) gauge field and the other two degenerate modes being protected by point-group symmetries. Our findings extend the search for the PC state from strongly correlated solid-state materials to weakly interacting Bose gases.

*hwachanphy@zjnu.edu.cn

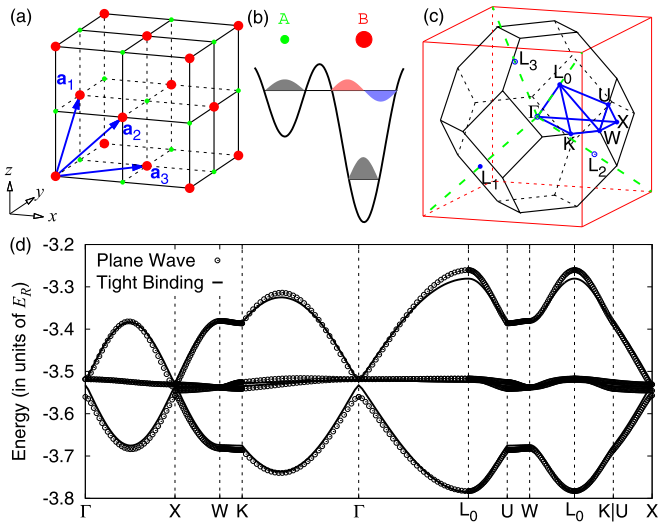

FIG. 1. (a) The fcc Bravais lattice with primitive lattice vectors. (b) Schematic plot of the orbital configuration in the $\mathcal{A}$ and $\mathcal{B}$ sublattices. (c) Brillouin zone of the fcc lattice with high-symmetry lines and points indicated. (d) Band structures with plane-wave expansions (open circles) and tight-binding approximations (solid lines) for the optical potentials $\{V, \Delta V\} = \{-5E_R, -0.9623E_R\}$ in Eq. (1) along the high-symmetry lines indicated in (c). The recoil energy is defined as $E_R = \pi^2\hbar^2/2md^2$.

The remainder of this paper is organized as follows. In Sec. II we introduce the optical potential for the fcc lattice. The band structure is solved with plane-wave expansions. A four-band tight-binding model is also constructed to capture the low-energy spectrum. In Sec. III the classical ground states in the weak-coupling limit are obtained within the Gross-Pitaevskii approximation. The quantum and thermal fluctuations are further considered to lift the degeneracy of classical ground states. Finally, we summarize our results and discuss the possible experimental detection in Sec. IV.

II. SINGLE-PARTICLE PHYSICS

We start with the optical potential for the fcc lattice [32,33]

$$\mathcal{V}(\boldsymbol{r}) = V\sum_{i=1}^{3}\cos(\bar{\boldsymbol{b}}_i\cdot\boldsymbol{r}) + \Delta V\sum_{i=0}^{3}\cos(\boldsymbol{b}_i\cdot\boldsymbol{r}), \tag{1}$$

where $\boldsymbol{b}_1 = \pi(-\hat{x}+\hat{y}+\hat{z})/d$, $\boldsymbol{b}_2 = \pi(\hat{x}-\hat{y}+\hat{z})/d$, and $\boldsymbol{b}_3 = \pi(\hat{x}+\hat{y}-\hat{z})/d$ are the reciprocal lattice vectors with d the lattice spacing, $\boldsymbol{b}_0 = -\sum_{i=1}^{3}\boldsymbol{b}_i$, and $\bar{\boldsymbol{b}}_i = \boldsymbol{b}_0 + \boldsymbol{b}_i$. The optical potential in Eq. (1) produces a three-dimensional bipartite lattice structure with ΔV dictating the staggered potential difference between $\mathcal{A}$ and $\mathcal{B}$ sublattices shown in Figs. 1(a) and 1(b). Without loss of generality, we will restrict our discussion below to $V < 0$ and $\Delta V < 0$. As depicted in Fig. 1(b), we focus on the case that the $\mathcal{B}$ sublattice is much deeper than the $\mathcal{A}$ sublattice such that the former hosts $\boldsymbol{p} \equiv (p_x, p_y, p_z)$ orbitals, while the latter hosts s orbitals. The low-lying s orbitals in sublattice $\mathcal{B}$ are well separated from the $\boldsymbol{p}$ orbitals in energy and thus can be safely neglected. The local minimum of the optical potential in Eq. (1) underlies a fcc Bravais lattice depicted in Fig. 1(a). The band structure is first solved by the plane-wave expansions (see Appendix A for details). The calculated band structure is shown in Fig. 1(d) and has degenerate band minima at four distinct momenta $\boldsymbol{L}_{i=\{0,1,2,3\}} = -\boldsymbol{b}_i/2$ in the first Brillouin zone.

To facilitate our understanding, the tight-binding model is desired to capture the band dispersion from plane-wave expansions. The minimal tight-binding model consists of the σ bonds $t_{\alpha\beta\sigma}$ between α and β orbitals up to the second-nearest-neighbor sites as well as the on-site energies of s and $\boldsymbol{p}$ orbitals. The π bond $t_{pp\pi}$ lies in the nodal plane of the p orbitals and is typically much weaker than the σ bond $t_{pp\sigma}$. Thus, for practical consideration, we neglect the π bonding in the tight-binding approximation. We next address the on-site energies of the s and $\boldsymbol{p}$ orbitals taking into consideration symmetry aspects [34]. Switching to spherical coordinates, the optical potential in Eq. (1) around $\mathcal{A}$ $(-)$ and $\mathcal{B}$ $(+)$ sublattices can be expressed as

$$\begin{aligned}\mathcal{V}(\boldsymbol{r}) &= \sum_{\ell\ \text{even}}\sum_{m=-\ell}^{\ell} 4\pi i^{\ell} v^{\pm}_{\ell m}(r) Y_{\ell m}(\hat{\boldsymbol{r}}),\\ v^{\pm}_{\ell m}(r) &\equiv \sum_{i=1}^{3} V\, j_{\ell}(\bar{b}_i r) Y^{*}_{\ell m}(\hat{\bar{\boldsymbol{b}}}_i)\\ &\quad \pm \sum_{i=0}^{3}\Delta V\, j_{\ell}(b_i r) Y^{*}_{\ell m}(\hat{\boldsymbol{b}}_i),\end{aligned} \tag{2}$$

where $j_\ell(z)$ is the spherical Bessel function of the first kind and $Y_{\ell m}(\hat{\boldsymbol{r}})$ is the spherical harmonic function. The s orbital has zero angular momentum and only receives a nonzero correction from the isotropic channel $\ell = 0$, which is predicted by the section rule on the orbital angular momentum [34]. In contrast, the $\boldsymbol{p}$ orbitals form an $\ell = 1$ angular momentum and thus receive possible corrections from $\ell = 0, 2$ channels. Direct evaluation shows that the $v^{+}_{\ell=2,m}(r)$ in Eq. (2) vanishes. Therefore, the $\boldsymbol{p}$ orbitals receive nonzero corrections only from the isotropic channel $\ell = 0$ and therefore remain degenerate. With these in mind, we denote the on-site energies of s and $\boldsymbol{p}$ orbitals by ϵ_s and ϵ_p, respectively. Introducing a spinor representation for the Bloch field operator $\psi_{\boldsymbol{k}} = (s_{\boldsymbol{k}}, p_{x\boldsymbol{k}}, p_{y\boldsymbol{k}}, p_{z\boldsymbol{k}})^{\mathsf{T}}$, the tight-binding model in momentum space is then given by

$$H_{\mathrm{TB}} = \sum_{\boldsymbol{k}} \psi^{\dagger}_{\boldsymbol{k}}\mathcal{H}_{\boldsymbol{k}}\psi_{\boldsymbol{k}}, \tag{3}$$

where

$$\mathcal{H}_{\boldsymbol{k}} = \begin{pmatrix} \xi_s & 2it_{sp\sigma}s_x & 2it_{sp\sigma}s_y & 2it_{sp\sigma}s_z \\ -2it_{sp\sigma}s_x & \xi_x & -2t_{pp\sigma}s_xs_y & -2t_{pp\sigma}s_zs_x \\ -2it_{sp\sigma}s_y & -2t_{pp\sigma}s_xs_y & \xi_y & -2t_{pp\sigma}s_ys_z \\ -2it_{sp\sigma}s_z & -2t_{pp\sigma}s_zs_x & -2t_{pp\sigma}s_ys_z & \xi_z \end{pmatrix},$$

with $s_\mu \equiv \sin k_\mu$, $\xi_s \equiv \sum_{\mu\nu}^{\mu\neq\nu} t_{ss\sigma}\cos k_\mu\cos k_\nu + \epsilon_s$, and $\xi_\mu \equiv \sum_{\nu\neq\mu} 2t_{pp\sigma}\cos k_\mu\cos k_\nu + \epsilon_p$. It is worth noting that the relative difference $\epsilon_s - \epsilon_p$ between the on-site energies of s and $\boldsymbol{p}$ orbitals can be continuously tuned through the optical potential ΔV in Eq. (1). In the band-fitting procedure, the optical potentials in units of recoil energy $E_R = \pi^2\hbar^2/2md^2$ are chosen as $\{V, \Delta V\} = \{-5E_R, -0.9623E_R\}$ such that the on-site energies of s and $\boldsymbol{p}$ orbitals are degenerate $\epsilon_s = \epsilon_p \equiv \epsilon$, which

greatly simplifies our analysis below. Here we emphasize that the physics we discussed does not sensitively depends on the parameters. As shown in Fig. 1(d), the fitted tight-binding model produces well the overall band dispersion from the plane-wave expansions and faithfully captures the low-energy behavior around the band minima.[1] With the constructed tight-binding model, the quasiparticles of the degenerate band minima have energy $\epsilon_{\boldsymbol{L}} = -2\sqrt{3t_{sp\sigma}^2 + t_{pp\sigma}^2} - 2t_{pp\sigma} + \epsilon$ and are given by

$$\psi_{\boldsymbol{L}_i}^\dagger = \cos\Phi s_{\boldsymbol{L}_i}^\dagger + i\sin\Phi \hat{\boldsymbol{L}}_i \cdot \boldsymbol{p}_{\boldsymbol{L}_i}^\dagger, \quad i = \{0,1,2,3\}, \tag{4}$$

where $\Phi = \arctan\Upsilon$ with the auxiliary function $\Upsilon \equiv (t_{pp\sigma} + \sqrt{t_{pp\sigma}^2 + 3t_{sp\sigma}^2})/\sqrt{3}t_{sp\sigma}$. Based on these quasiparticles, a set of degenerate single-particle states that equally minimize the kinetic energy can be constructed by linear superposition of the band minima $\psi^\dagger = \sum_{i=0}^3 \phi_i \psi_{\boldsymbol{L}_i}^\dagger$. Its manifold exists on the surface S^7 in $\mathbb{R}^8$, $|\boldsymbol{\phi}| = 1$, with $\boldsymbol{\phi} \equiv (\phi_0, \phi_1, \phi_2, \phi_3)$. Because of the infinite degeneracy of the single-particle states, free bosons cannot be condensed.

III. WEAKLY INTERACTING MANY-PARTICLE PHYSICS

A. Classical ground state

Having established the single-particle physics, we are then in a position to study how the many-body interaction lifts the infinite degeneracy of single-particle states. The on-site Hubbard interactions can be experimentally realized through the s-wave Feshbach resonance [35] and take the form

$$H_{\rm I} = \frac{U_s}{2}\sum_{\boldsymbol{r}} \hat{n}_{s\boldsymbol{r}}(\hat{n}_{s\boldsymbol{r}} - 1) + \frac{U_p}{2}\sum_{\boldsymbol{r}}\left[\hat{n}_{p\boldsymbol{r}}^2 - \frac{\hat{n}_{p\boldsymbol{r}} + \hat{\boldsymbol{J}}_{\boldsymbol{r}}^2}{3}\right], \tag{5}$$

where $\hat{n}_{s\boldsymbol{r}} = s_{\boldsymbol{r}}^\dagger s_{\boldsymbol{r}}$ and $\hat{n}_{p\boldsymbol{r}} = \sum_\mu p_{\mu\boldsymbol{r}}^\dagger p_{\mu\boldsymbol{r}}$ are the density operators for s and $\boldsymbol{p}$ orbitals, respectively, the μ-component orbital angular momentum operator $\hat{J}_{\boldsymbol{r}}^\mu = -i\sum_{\nu\lambda}\epsilon_{\mu\nu\lambda} p_{\nu\boldsymbol{r}}^\dagger p_{\lambda\boldsymbol{r}}$, and $\epsilon_{\mu\nu\lambda}$ is the Levi-Cività symbol. The interaction parameters can be estimated as $U_s = \frac{4}{3}[1 - 2\Delta V/(V + \Delta V)]^{3/2}U_p \equiv U$ from the harmonic approximation [36,37]. The last term in Eq. (6) has SU(2) rotational symmetry and favors spontaneous orbital angular momenta to lower the energy, which is analogous to Hund's coupling for electrons in an atom. According to the orbital Hund's rule, the bosons are not subject to the Pauli exclusion principle and tend to condensate in a single orbital to maximize the orbital angular momentum.

We next turn to the many-particle wave function of the condensates. It is worth mentioning that the fragmented condensate violates the orbital Hund's rule and does not optimize the orbital Hund's coupling due to the exchange correlations [38]. Below we will consider the coherent condensate $|\Psi\rangle = \frac{1}{\sqrt{\mathcal{N}_0!}}(\sum_{i=0}^3 \phi_i \psi_{\boldsymbol{L}_i}^\dagger)^{\mathcal{N}_0}|0\rangle$, where $|0\rangle$ denotes the vacuum state and $\mathcal{N}_0$ is the number of condensed bosons. Using the coherent state, the time-dependent Gross-Pitaevskii equation can be readily derived through the Euler-Lagrange equation [39]

$$\frac{\partial\mathcal{L}}{\partial\phi_i^*} - \frac{d}{dt}\left(\frac{\partial\mathcal{L}}{\partial\dot{\phi}_i^*}\right) = 0, \quad i = \{0,1,2,3\}, \tag{6}$$

where the Lagrangian $\mathcal{L} \equiv \sum_{i=0}^3 i\frac{\hbar}{2}(\phi_i^*\dot{\phi}_i - \phi_i\dot{\phi}_i^*) - \mathcal{E}(\boldsymbol{\phi}^*, \boldsymbol{\phi})$, with $\mathcal{E}(\boldsymbol{\phi}^*, \boldsymbol{\phi}) \equiv \langle\Psi|H_{\rm TB} + H_{\rm I}|\Psi\rangle/\mathcal{N}_{\rm L}$ the energy functional and $\mathcal{N}_{\rm L}$ the number of lattice sites. The derivation of the Gross-Pitaevskii equation is presented in Appendix B. Here we briefly discuss the symmetry. As shown in Fig. 2(a), $\boldsymbol{L}_{0,1,2,3}$ connect the center of a tetrahedron to its vertices. The Lagrangian $\mathcal{L}$ naturally inherits the T_d point-group symmetry of the tetrahedron through the single-particle states in Eq. (5). The Gross-Pitaevskii equation is numerically solved with the imaginary-time evolution by propagating an initial trial state [40]. With different initial states, a series of degenerate ground states is obtained. We illustrate the ground-state configuration $\boldsymbol{\phi}$ by several sets of numerical solutions depicted in Fig. 2(b). The configuration $\boldsymbol{\phi}$ splits into two pairs with identical complex moduli. The complex phases of $\boldsymbol{\phi}$ also have internal structures: Two ϕ's have identical phases and the others are $\pi/2$ ahead and behind. With these insights, the numerical solutions can be described by the analytic expression [up to a global U(1) phase]

$$\boldsymbol{\phi} = \frac{1}{\sqrt{2}}(i\cos\theta, \cos\theta, -i\sin\theta, \sin\theta), \quad 0 \leqslant \theta < \pi, \tag{7}$$

or its counterparts with permutations, which is a manifestation of T_d point-group symmetry [41]. Moreover, we have also verified that the ground-state energy density in numerical simulations is consistent with the analytic result $\mathcal{E}_0 = \epsilon_{\boldsymbol{L}} n_0 + (\cos^4\Phi U_s + 19\sin^4\Phi U_p/27)n_0^2/2$, where the condensation density $n_0 = \mathcal{N}_0/\mathcal{N}_{\rm L}$. The ground states spontaneously break the time-reversal symmetry and support p-orbital angular momenta due to the aforementioned orbital Hund's coupling. The p-orbital angular momenta involve the interference between the band minima at $\boldsymbol{L}_{\{0,1,2,3\}}$, resulting in a reduced Brillouin zone in Fig. 2(a). With the analytic configuration in Eq. (7), the trajectories of p-orbital angular momenta $\boldsymbol{J}_{\boldsymbol{r}}$ plotted in Fig. 2(c) have an enlarged unit cell with four sublattices forming a tetrahedron, which we have confirmed also in the numerical simulations. The classical solution of the Gross-Pitaevskii equation partially lifts the single-particle degeneracy on the surface S^7 and still has infinite degeneracy arising from the global U(1) phase and the continuous symmetry characterized by θ in Eq. (7). The classical ground-state degeneracy is a consequence of geometric frustration, i.e., the inability to simultaneously minimize the energy of all bonds in the superlattice composed of emergent tetrahedra.

B. Quantum ground state

The ground states of the Gross-Pitaevskii equation can evolve in the continuous symmetry space without energy cost, e.g., the trajectories in Fig. 2(c), which makes the system particularly susceptible to fluctuations. We therefore proceed to examine the effects of fluctuations on the degenerated classical ground states. Following the standard Bogoliubov approximation for a weakly interacting Bose gas [42,43], the bosonic field $\psi_{\boldsymbol{L}_i+\boldsymbol{k}}$ around the band minima $\boldsymbol{L}_i$ is separated into the classical condensation ϕ_i and the fluctuating field $\phi_{i\boldsymbol{k}}$ as $\psi_{\boldsymbol{L}_i+\boldsymbol{k}} = \phi_i + \phi_{i\boldsymbol{k}}$. We further project both the kinetic and interaction terms into the four lowest branches at the band minima, which captures the essential low-energy physics in the long-wavelength limit. Within the formalism of the

[1]The fitting parameters are given by $\{t_{sp\sigma}, t_{ss\sigma}, t_{pp\sigma}, \epsilon\} = \{0.073E_{\rm R}, -0.0006E_{\rm R}, 0.002E_{\rm R}, -3.529E_{\rm R}\}$.

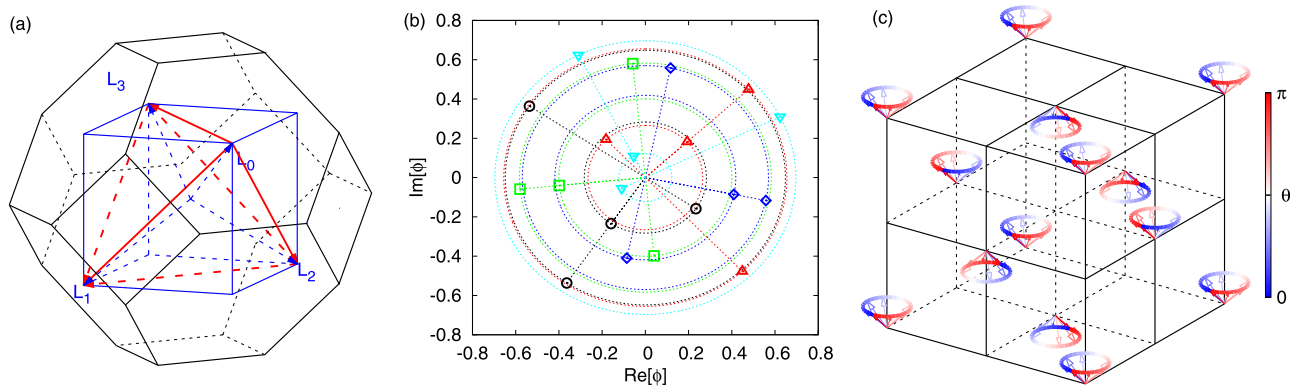

FIG. 2. (a) The inner blue cube denotes the magnetic Brillouin zone of p-orbital angular momenta in (c) due to the interference of condensates at momenta $\boldsymbol{L}_{\{0,1,2,3\}}$. (b) Illustration of the ground-state configurations $\boldsymbol{\phi} = (\phi_0, \phi_1, \phi_2, \phi_3)$ obtained by the imaginary-time evolution of the Gross-Pitaevskii equation. Different initial configurations in the numerical simulations are indicated by point types. (c) Trajectories of spontaneous p-orbital angular momenta with the color encoding the angle θ in Eq. (7).

functional integral, the partition function is given by

$$\mathcal{Z} = \int \mathcal{D}[\bar{\boldsymbol{\phi}}, \boldsymbol{\phi}] e^{-\mathcal{S}_{\rm eff}[\bar{\boldsymbol{\phi}}, \boldsymbol{\phi}]}, \tag{8}$$

where the effective action up to quadratic order reads

$$\mathcal{S}_{\rm eff}[\bar{\boldsymbol{\phi}}, \boldsymbol{\phi}] = \frac{1}{2}\sum_k (\bar{\boldsymbol{\phi}}_k \quad \boldsymbol{\phi}_{-k}) \mathcal{G}_k^{-1} \begin{pmatrix} \boldsymbol{\phi}_k \\ \bar{\boldsymbol{\phi}}_{-k} \end{pmatrix} - \sum_{\boldsymbol{k}} \frac{{\rm Tr}\mathcal{G}_{\boldsymbol{k},0}^{-1}}{4},$$

$$\mathcal{G}_k^{-1} = \begin{pmatrix} -i\omega_n + \epsilon_{\boldsymbol{k}} + \boldsymbol{\Sigma} & \boldsymbol{\Delta} \\ \boldsymbol{\Delta}^\dagger & i\omega_n + \epsilon_{-\boldsymbol{k}} + \boldsymbol{\Sigma}^{\rm T} \end{pmatrix},$$

$$k \equiv (\boldsymbol{k}, \omega_n)$$

(see Appendix C for the derivation). Here we have defined the auxiliary matrices

$$\boldsymbol{\Sigma} = \{\mathcal{U}_s + 11\mathcal{U}_p\}\mathbf{1} + 8\mathcal{U}_p\{\cos(2\theta)\gamma^0 + i\sin(2\theta)\sigma^{03}\},$$

$$\boldsymbol{\Delta} = \mathcal{U}_s\{\sin(2\theta)\gamma^5 + i\cos(2\theta)\sigma^{23}\} + \mathcal{U}_p\{4i\gamma^1\gamma^5 - 4\sigma^{12} + \sin(2\theta)(7\gamma^5 - 4\gamma^2) + \cos(2\theta)(7\sigma^{23} - 4\gamma^3\gamma^5)\},$$

with gamma matrices $\gamma^{0,1,2,3,5}$ in the Pauli-Dirac representation, $\sigma^{\mu\nu} = \frac{i}{2}[\gamma^\mu, \gamma^\nu]$, the effective interaction parameters $\{\mathcal{U}_s, \mathcal{U}_p\} = \{U_s n\cos^4\Phi, U_p n \sin^4\Phi/27\}$, and the total density of bosons n. The band dispersions $\epsilon_{\boldsymbol{k}} = {\rm diag}(\epsilon_{0\boldsymbol{k}}, \epsilon_{1\boldsymbol{k}}, \epsilon_{2\boldsymbol{k}}, \epsilon_{3\boldsymbol{k}})$ are expanded in small $\boldsymbol{k}$ around the band minima and are given by

$$\epsilon_{i\boldsymbol{k}} = \beta|\boldsymbol{k}|^2 + \beta'(k_y k_z, k_z k_x, k_x k_y)\cdot\hat{\boldsymbol{L}}_i + O(|\boldsymbol{k}|^4), \tag{9}$$

with $\{\beta, \beta'\} = \{t_{sp\sigma}/\sqrt{3} + t_{pp\sigma}, -2(t_{pp\sigma}/\sqrt{3} + \sqrt{3}t_{ss\sigma})\}$. The σ bonds $t_{ss\sigma/pp\sigma}$ between second nearest neighbors are relatively weak. In Eq. (9) we keep up to the linear order in $t_{ss\sigma/pp\sigma}$. A remarkable feature of the second term in Eq. (9) is the anisotropy, which will be discussed later. Below we will first focus on the isotropic case $\beta' = 0$. The excitation spectrum $\omega_{i\boldsymbol{k}}$ is determined by the poles of the Green's function ${\rm det}\mathcal{G}_k^{-1} = 0$ with an inverse Wick rotation $i\omega_n \to \omega_{\boldsymbol{k}}$. In the long-wavelength limit, the excitation spectrum for $\theta \neq \mathbb{Z}\pi/4$ features two linearly dispersing NG modes, arising from the breaking of the aforementioned continuous symmetries. In contrast, at $\theta = 0, \pi/2$ and $\theta = \pi/4, 3\pi/4$, the lattice exhibits a periodic repetition of the collinear antiferromagnetic (CAFM) and PC ordering of p-orbital angular momenta shown in Figs. 3(a) and 3(b), respectively. The CAFM and PC orderings preserve the σ_d and S_4 symmetries of the T_d point group and have an additional NG mode as a consequence

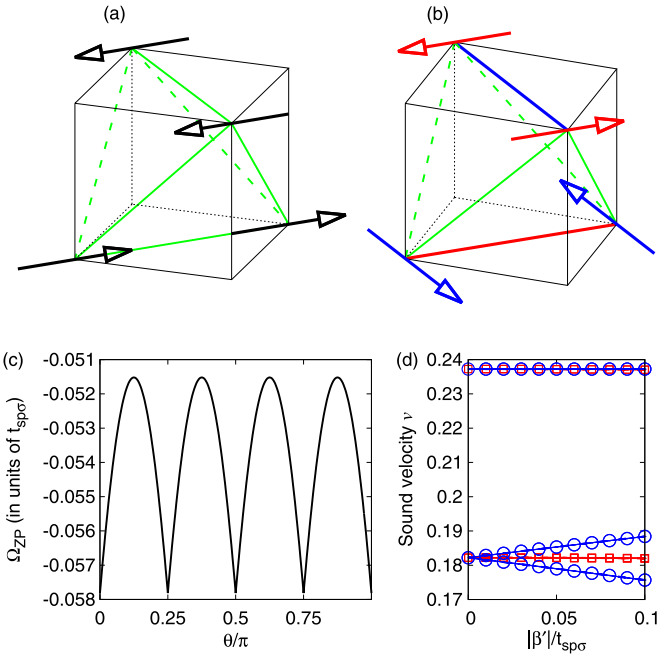

FIG. 3. Schematic plot of the ordering pattern of p-orbital angular momenta on a single tetrahedron for (a) collinear antiferromagnetic ordering at $\theta = 0, \pi/2$ and (b) Palmer-Chalker ordering at $\theta = \pi/4, 3\pi/4$ (the p-orbital angular momenta are the same color as the parallel edges of tetrahedron). (c) Thermodynamic potential from the zero-point fluctuation $\Omega_{\rm ZP}$ in the long-wavelength limit with $\{\beta, \beta', U, n\} = \{t_{sp\sigma}/\sqrt{3}, 0, t_{sp\sigma}/10, 1\}$. (d) Numerical evaluation on the solid-angle averaged sound velocities of Nambu-Goldstone modes for the collinear antiferromagnetic (open red squares) and Palmer-Chalker (open blue circles) states with $\{\beta, U, n\} = \{t_{sp\sigma}/\sqrt{3}, t_{sp\sigma}/10, 1\}$. For the isotropic case $\beta' = 0$, we have also numerically confirmed that the sound velocities of Nambu-Goldstone modes are θ independent.

of breaking the continuous symmetry of the σ_d and S_4 counterparts in Eq. (7), respectively. This result is also supported by our analytical calculations at $\theta = \mathbb{Z}\pi/4$. The CAFM and PC states share an identical spectrum, two degenerate gapless modes with sound velocity $v = \sqrt{2t_{sp\sigma}(\mathcal{U}_s + 3\mathcal{U}_p)}/\sqrt[4]{3}$ and the other one with velocity $v = \sqrt{2t_{sp\sigma}(\mathcal{U}_s + 19\mathcal{U}_p)}/\sqrt[4]{3}$. It is worth mentioning that the ordering of p-orbital angular momenta is a manifestation of the relative phases between orbitals and they share the same point-group symmetry. For arbitrary θ, analytical results are no longer available. The numerical evaluation of the sound velocities of NG modes suggests that the velocities are θ independent within numerical resolutions. We next turn to discuss the thermodynamic potential $\Omega = -T \ln \mathcal{Z} = \Omega_{\rm ZP} + \Omega_{\rm T}$, originating from the zero-point fluctuation $\Omega_{\rm ZP} = \sum_{\boldsymbol{k}}(\sum_i 2\omega_{i\boldsymbol{k}} - {\rm Tr}\mathcal{G}^{-1}_{\boldsymbol{k},0})/4$ and the thermal fluctuation $\Omega_{\rm T} = T\sum_{i\boldsymbol{k}} \ln[1 - \exp(-\beta\omega_{i\boldsymbol{k}})]$. Since the effective action is only valid in the long-wavelength limit, the zero-point fluctuation in this limit is shown in Fig. 3(c) and favors both the CAFM and PC states, which further confirms our previous analysis of NG modes in terms of symmetry aspects. At low temperatures, the thermal fluctuation of the thermodynamic potential is dominated by NG modes $\omega_{\boldsymbol{k}} = v|\boldsymbol{k}|$ with the contributions following a power-law behavior $\Omega_{\rm T} \propto -T^4/v^3$. The CAFM and PC states both possess three NG modes and thus have a lower thermodynamic potential due to the entropic gain from the zero-point motion of NG modes through thermal fluctuations. Finally, we would like to discuss the anisotropy induced by the intraorbital σ bonds $t_{ss\sigma/pp\sigma}$ in Eq. (9). The anisotropy β' with the present fitting parameters is weak; however, it can be enhanced through tuning the staggered potential ΔV in Eq. (1). Hence we release β' as a free parameter. The anisotropic sound velocities are numerically evaluated by averaging over the solid angle of $\boldsymbol{k}$ and are found to be independent of the sign of β'. As shown in Fig. 3(d), the averaged sound velocities of the degenerate NG modes in the PC state are split into two branches, with the low-lying one well below those in the CAFM state. The Bogoliubov excitation corresponds to simultaneous creation or annihilation of two bosons in the excited states with the momentum $\pm\boldsymbol{k}$ relation to the band minima. The band anisotropy in Eq. (9) is characterized by the crystal momentum $\hat{\boldsymbol{L}}_i$ around the band minimum $\boldsymbol{L}_i$. One distinction between the CAFM and PC states is that the PC state involves the Bose condensation at four band minima and the CAFM state involves only two of the four band minima. For the PC state, the Bogoliubov spectrum corresponds to the excitation on top of the Bose condensation at four crystal momenta $\boldsymbol{L}_i$ and naturally inherits the band anisotropy. By averaging over the solid angle of $\boldsymbol{k}$, the PC state has a lower branch of NG modes than the CAFM state and is selected as the quantum ground state through thermal fluctuations.

IV. CONCLUSION

For weakly interacting Bose gases, we have predicted that the PC instability can be induced by both quantum and thermal fluctuations in a fcc optical lattice. Remarkably, our weak-coupling approach combined with numerical and analytical calculations is also applicable to a generic bosonic superfluidity with multiple degenerate minima in its single-particle spectrum. We would like to briefly discuss the experimental detection. Based on the current experimental techniques in ultracold atoms, the momentum distribution of Bose condensates can be measured by the time-of-flight technique with a sudden expansion of the trapped condensates [44–47]. The crystal momentum distribution in the first Brillouin zone can be constructed based on the bare momentum distribution [48]. The PC state is uniquely characterized by the identical intensity at the corners of magnetic Brillouin zone in Fig. 2(a). In addition, the NG modes, as the hallmark of continuous symmetry breaking, can be directly detected by momentum-resolved Bragg spectroscopy [49]. We hope that our work will open new avenues to simulate the strongly correlated magnetic states in solid-state materials using weakly interacting Bose gases in optical lattices.

ACKNOWLEDGMENTS

The author is grateful to X. Li for helpful discussions. This work was supported by National Natural Science Foundation of China under Grants No. 11704338 and No. 11835011.

APPENDIX A: BAND STRUCTURE CALCULATION WITH PLANE-WAVE EXPANSIONS

In this Appendix we solve the band structure of the Hamiltonian

$$\hat{\mathcal{H}}_{\rm OL} = \int d\boldsymbol{r}\, \hat{\Psi}^\dagger(\boldsymbol{r})\left[-\frac{\hbar^2}{2m}\nabla^2 + \mathcal{V}(\boldsymbol{r})\right]\hat{\Psi}(\boldsymbol{r}) \tag{A1}$$

with plane-wave expansions [50]. For fcc optical lattice, the optical potential $\mathcal{V}(\boldsymbol{r}+\boldsymbol{R}) = \mathcal{V}(\boldsymbol{r})$ is invariant under discrete translation vectors $\boldsymbol{R} = N_1\boldsymbol{a}_1 + N_2\boldsymbol{a}_2 + N_3\boldsymbol{a}_3$ with integer multiples of three primitive vectors

$$\boldsymbol{a}_1 = d(\hat{y}+\hat{z}), \quad \boldsymbol{a}_2 = d(\hat{z}+\hat{x}), \quad \boldsymbol{a}_3 = d(\hat{x}+\hat{y}), \tag{A2}$$

where d is the lattice spacing. Making use of Bloch's theorem, the field operator in Eq. (A1) is represented as $\hat{\Psi}(\boldsymbol{r}) = \sum_{n\boldsymbol{k}} \psi_{n\boldsymbol{k}}(\boldsymbol{r})\hat{\Psi}_{n\boldsymbol{k}}$ with the Bloch wave function

$$\psi_{n\boldsymbol{k}}(\boldsymbol{r}) \equiv \exp(i\boldsymbol{k}\cdot\boldsymbol{r})\phi_{n\boldsymbol{k}}(\boldsymbol{r}), \tag{A3}$$

where the quantum number n is the band index and the crystal momentum $\boldsymbol{k}$ can be composed of the reciprocal lattice vectors with fractional coefficients

$$\boldsymbol{k} = k_1\boldsymbol{b}_1 + k_2\boldsymbol{b}_2 + k_3\boldsymbol{b}_3 \tag{A4}$$

and the reciprocal lattice vectors

$$\begin{aligned}\boldsymbol{b}_1 &= \frac{\pi}{d}(-\hat{x}+\hat{y}+\hat{z}),\\ \boldsymbol{b}_2 &= \frac{\pi}{d}(\hat{x}-\hat{y}+\hat{z}),\\ \boldsymbol{b}_3 &= \frac{\pi}{d}(\hat{x}+\hat{y}-\hat{z}).\end{aligned} \tag{A5}$$

The Bloch orbitals $\phi_{n\boldsymbol{k}}(\boldsymbol{r})$ in Eq. (A3) inherit the periodicity of the lattice potential, i.e., $\phi_{n\boldsymbol{k}}(\boldsymbol{r}+\boldsymbol{R}) = \phi_{n\boldsymbol{k}}(\boldsymbol{r})$. Therefore, the Bloch wave function can be further rewritten as a linear

combination of plane waves

$$\psi_{n\boldsymbol{k}}(\boldsymbol{r}) = \sum_{\mathbf{G}} \exp[i(\boldsymbol{k}+\mathbf{G})\cdot\boldsymbol{r}]\phi^{\mathbf{G}}_{n\boldsymbol{k}} \tag{A6}$$

with plane-wave vectors $\mathbf{G} = \mathrm{G}_1\boldsymbol{b}_1 + \mathrm{G}_2\boldsymbol{b}_2 + \mathrm{G}_3\boldsymbol{b}_3$. Taking the orthogonality of Bloch wave functions, the eigenstates of the Hamiltonian in Eq. (A1) can be recast in a coupled set of matrix eigenvalue equations

$$4E_{\mathrm{R}}(\boldsymbol{k}+\mathbf{G})^2\phi^{\mathbf{G}}_{n\boldsymbol{k}} + \sum_{\mathbf{G}'} V(\mathbf{G}-\mathbf{G}')\phi^{\mathbf{G}'}_{n\boldsymbol{k}} = \epsilon_{n\boldsymbol{k}}\phi^{\mathbf{G}}_{n\boldsymbol{k}}, \tag{A7}$$

where the recoil energy $E_{\mathrm{R}} = \pi^2\hbar^2/2md^2$. The Fourier transform of lattice potential is given by

$$V(\mathbf{G}) = \frac{1}{V_{\mathrm{uc}}}\int_{\text{unit cell}} d^3\boldsymbol{r}\,\mathcal{V}(\boldsymbol{r})\exp(-i\mathbf{G}\cdot\boldsymbol{r}), \tag{A8}$$

where $V_{\mathrm{uc}} = |\boldsymbol{a}_1\cdot(\boldsymbol{a}_2\times\boldsymbol{a}_3)|$ is the volume of the primitive unit cell.

APPENDIX B: DERIVATION OF THE TIME-DEPENDENT GROSS-PITAEVSKII EQUATION

The time-dependent Gross-Pitaevskii equation is obtained by neglecting the quantum fluctuations of the operators and replacing them by c numbers, which are usually the averages of operators in the ground state. We consider the coherent condensed wave function of an ideal Bose gas

$$|\Psi\rangle = \frac{1}{\sqrt{\mathcal{N}_0!}}\left(\sum_{i=0}^{3}\phi_i\psi^{\dagger}_{\boldsymbol{L}_i}\right)^{\mathcal{N}_0}|0\rangle, \tag{B1}$$

where $|0\rangle$ denotes the vacuum state and $\mathcal{N}_0$ is the number of condensed bosons. The condensed boson density is given by $n_0 = \frac{\mathcal{N}_0}{\mathcal{N}_{\mathrm{L}}}$, with $\mathcal{N}_L$ the number of lattice sites. The thermodynamic limit is defined by taking the limit $\mathcal{N}_0\to\infty$ and $\mathcal{N}_{\mathrm{L}}\to\infty$ with fixed density n_0. In the Gross-Pitaevskii approximation, the operators $\psi_{\boldsymbol{L}_i}$ are replaced by c numbers

$$\psi_{\boldsymbol{L}_i} \to \sqrt{\mathcal{N}_0}\phi_i. \tag{B2}$$

Accordingly, the operators $s_{\boldsymbol{L}_i}$ and $p_{\mu\boldsymbol{L}_i}$ are approximated as

$$s_{\boldsymbol{L}_i} \to \sqrt{\mathcal{N}_0}\phi_i\cos\Phi, \tag{B3}$$

$$p_{\mu\boldsymbol{L}_i} \to i\sqrt{\mathcal{N}_0}\phi_i\sin\Phi\hat{\boldsymbol{L}}^{\mu}_i. \tag{B4}$$

After lengthy but straightforward algebra, the Lagrangian can be written as

$$\mathcal{L} \equiv \sum_i i\frac{\hbar}{2}(\phi^*_i\dot{\phi}_i - \phi_i\dot{\phi}^*_i) - \mathcal{E}(\boldsymbol{\phi}^*,\boldsymbol{\phi}), \tag{B5}$$

where the energy functional

$$\mathcal{E}(\boldsymbol{\phi}^*,\boldsymbol{\phi}) \equiv \frac{1}{\mathcal{N}_{\mathrm{L}}}[\langle\Psi|H_{\mathrm{TB}}|\Psi\rangle + \langle\Psi|H_{\mathrm{I}}|\Psi\rangle], \tag{B6}$$

with

$$\langle\Psi|H_{\mathrm{TB}}|\Psi\rangle = \mathcal{N}_0\Big[-2\Big(\sqrt{2t^2_{sp\sigma}+t^2_{pp\sigma}}+t_{pp\sigma}\Big)+\epsilon\Big] \times\sum_i\phi^*_i\phi_i \equiv \mathcal{N}_0\epsilon_{\boldsymbol{L}}\sum_i\phi^*_i\phi_i, \tag{B7}$$

$$\langle\Psi|H_{\mathrm{I}}|\Psi\rangle = \frac{n_0}{2}\mathcal{N}_0U_s\cos^4\Phi\left(\sum_{ij}\phi^{*2}_i\phi^2_j + 2\sum_{i\neq j}\phi^*_i\phi_i\phi^*_j\phi_j + \sum_{(ijkl)}\phi^*_i\phi^*_j\phi_k\phi_l\right) + \frac{n_0}{6}\mathcal{N}_0U_p\sin^4\Phi\left(3\sum_i\phi^{*2}_i\phi^2_i + \frac{11}{9}\sum_{i\neq j}\phi^{*2}_i\phi^2_j + \frac{22}{9}\sum_{i\neq j}\phi^*_i\phi_i\phi^*_j\phi_j + \frac{1}{3}\sum_{(ijkl)}\phi^*_i\phi^*_j\phi_k\phi_l\right). \tag{B8}$$

Here $\epsilon_{\boldsymbol{L}} \equiv -2\sqrt{2t^2_{sp\sigma}+t^2_{pp\sigma}} - 2t_{pp\sigma} + \epsilon$ and $(ijkl)$ denotes all possible permutations of (0,1,2,3). Plugging Eq. (B5) into the Euler-Lagrange equation

$$\frac{\partial\mathcal{L}}{\partial\phi^*_i} - \frac{d}{dt}\left(\frac{\partial\mathcal{L}}{\partial\dot{\phi}^*_i}\right) = 0, \quad i=\{0,1,2,3\}, \tag{B9}$$

yields a set of coupled equations of motion [39]

$$i\hbar\dot{\phi}_i = \frac{\partial\mathcal{E}(\boldsymbol{\phi}^*,\boldsymbol{\phi})}{\partial\phi^*_i}, \quad i=\{0,1,2,3\}. \tag{B10}$$

The ground-state solution can be obtained by numerically evolving the imaginary-time equations of motion [51].

APPENDIX C: DERIVATION OF THE EFFECTIVE ACTION

In this Appendix we derive the low-energy effective action around the band minima at $\boldsymbol{L}_{0,1,2,3}$, which describes the quadratic fluctuation on top of the classical solution of the Gross-Pitaevskii equation. Following the standard Bogoliubov approximation, the bosonic field $\psi_{\boldsymbol{L}_i+\boldsymbol{k}}$ around the band minima $\boldsymbol{L}_i$ is separated into the classical condensation ϕ_i and the fluctuating field $\phi_{i\boldsymbol{k}}$ as $\psi_{\boldsymbol{L}_i+\boldsymbol{k}} = \phi_i + \phi_{i\boldsymbol{k}}$. The quadratic fluctuation includes the following three parts.

First, let us discuss the fluctuation arising from the energy functional of classical ground states. As illustrated in the main text, the configuration of the classical ground state is given by

$$\boldsymbol{\phi} = \frac{1}{\sqrt{2}}(i\cos\theta,\cos\theta,-i\sin\theta,\sin\theta). \tag{C1}$$

Substituting Eq. (C1) into the energy functional in Eq. (B6), we have

$$\mathcal{E}(\boldsymbol{\phi}^*,\boldsymbol{\phi}) = \epsilon_{\boldsymbol{L}}n_0 + \tfrac{1}{2}(\cos^4\Phi U_s + \tfrac{19}{27}\sin^4\Phi U_p)n^2_0, \tag{C2}$$

where the condensation density $n_0 = \mathcal{N}_0/\mathcal{N}_{\mathrm{L}}$. The total bosons consist of condensed bosons in the band minima and excited bosons in the fluctuating fields. Therefore, the conservation of bosons is given by

$$\mathcal{N} = \mathcal{N}_0 + \sum_{i\boldsymbol{k}}\phi^{\dagger}_{i\boldsymbol{k}}\phi_{i\boldsymbol{k}}. \tag{C3}$$

Substituting Eq. (C3) into the energy functional in Eq. (C2), the quadratic fluctuation can be expressed as

$$\mathcal{E}^{(2)}(\boldsymbol{\phi}^*,\boldsymbol{\phi}) = -\frac{1}{\mathcal{N}_\mathrm{L}}\left(\sum_{i\boldsymbol{k}}\phi^\dagger_{i\boldsymbol{k}}\phi_{i\boldsymbol{k}}\right) \times\left[\epsilon_{\boldsymbol{L}} + (\cos^4\Phi U_s + \frac{19}{27}\sin^4\Phi U_p)n\right], \quad \text{(C4)}$$

with n the total boson density.

Second, let us turn to the fluctuation from the tight-binding model. The band structures of the tight-binding model have four degenerate minima $\epsilon_{\boldsymbol{L}} = -2\sqrt{2t_{sp\sigma}^2 + t_{pp\sigma}^2} - 2t_{pp\sigma} + \epsilon$ at momenta $\boldsymbol{L}_{0,1,2,3}$. The eigenstates of the band minima at $\boldsymbol{L}_i$ are given by

$$\psi_i = [\cos\Phi, i\sin\Phi\hat{\boldsymbol{L}}_i^x, i\sin\Phi\hat{\boldsymbol{L}}_i^y, i\sin\Phi\hat{\boldsymbol{L}}_i^z]^\mathsf{T}. \quad \text{(C5)}$$

The effective low-energy band dispersions around the band minima are obtained by projecting the tight-binding model into the eigenstates in Eq. (C5) and take the form

$$\begin{aligned} E_{i\boldsymbol{k}} &= \langle\psi_i|\mathcal{H}_{\boldsymbol{L}_i+\boldsymbol{k}}|\psi_i\rangle \\ &= \epsilon_{\boldsymbol{L}} + \beta|\boldsymbol{k}|^2 + \beta'(k_yk_z, k_zk_x, k_xk_y)\cdot\hat{\boldsymbol{L}}_i + O(|\boldsymbol{k}|^4), \end{aligned} \quad \text{(C6)}$$

with $\{\beta,\beta'\} = \{t_{sp\sigma}/\sqrt{3} + t_{pp\sigma}, -2(t_{pp\sigma}/\sqrt{3} + \sqrt{3}t_{ss\sigma})\}$. In Eq. (C6) only the linear order in $t_{ss\sigma/pp\sigma}$ is kept. It is worth mentioning that we have verified that the second-order virtual process in which the boson first hops from the lowest band to the upper bands and then hops back to the lowest band contributes in order $|\boldsymbol{k}|^4$ and is thus neglected. Therefore, the quadratic fluctuation in the tight-binding model is given by

$$H^{(2)}_{\mathrm{TB}} = E_{i\boldsymbol{k}}\sum_{i\boldsymbol{k}}\phi^\dagger_{i\boldsymbol{k}}\phi_{i\boldsymbol{k}}. \quad \text{(C7)}$$

Finally, we discuss the fluctuation from the on-site Hubbard interaction. Let us illustrate the case for s orbitals first. The fluctuation for s orbitals takes the form

$$\begin{aligned} H^{(2)}_{\mathrm{I},s} &= \frac{U_s}{2}n\cos^2\Phi\sum_{\{i\}\boldsymbol{k}}\phi_{i_1}\phi_{i_2}s^\dagger_{\boldsymbol{L}_{i_3}+\boldsymbol{k}}s^\dagger_{\boldsymbol{L}_{i_4}-\boldsymbol{k}}\delta_{\boldsymbol{L}_{i_1}+\boldsymbol{L}_{i_2}-\boldsymbol{L}_{i_3}-\boldsymbol{L}_{i_4},\mathbf{G}} \\ &+ \frac{U_s}{2}n\cos^2\Phi\sum_{\{i\}\boldsymbol{k}}\phi^*_{i_1}\phi_{i_2}s^\dagger_{\boldsymbol{L}_{i_3}+\boldsymbol{k}}s_{\boldsymbol{L}_{i_4}+\boldsymbol{k}}\delta_{-\boldsymbol{L}_{i_1}+\boldsymbol{L}_{i_2}-\boldsymbol{L}_{i_3}+\boldsymbol{L}_{i_4},\mathbf{G}} \\ &+ \frac{U_s}{2}n\cos^2\Phi\sum_{\{i\}\boldsymbol{k}}\phi^*_{i_1}\phi^*_{i_2}s_{\boldsymbol{L}_{i_3}+\boldsymbol{k}}s_{\boldsymbol{L}_{i_4}-\boldsymbol{k}}\delta_{-\boldsymbol{L}_{i_1}-\boldsymbol{L}_{i_2}+\boldsymbol{L}_{i_3}+\boldsymbol{L}_{i_4},\mathbf{G}}. \end{aligned} \quad \text{(C8)}$$

Here we have replaced n_0 by n, which is correct to the order we are calculating. After projecting into the lowest band $s_{\boldsymbol{L}_i+\boldsymbol{k}} \approx \cos\Phi\phi_{i\boldsymbol{k}}$ and summation over $L_{\{i\}}$, lengthy but straightforward algebra leads to

$$\begin{aligned} H^{(2)}_{\mathrm{I},s} &= \frac{U_s}{2}n\cos^4\Phi\sum_{\boldsymbol{k}}\left[\sum_{ij}\phi_i\phi_i\phi^\dagger_{j\boldsymbol{k}}\phi^\dagger_{j-\boldsymbol{k}} + \sum_{i\neq j}2\phi_i\phi_j\phi^\dagger_{i\boldsymbol{k}}\phi^\dagger_{j-\boldsymbol{k}} + \sum_{(ijkl)}\phi_i\phi_j\phi^\dagger_{k\boldsymbol{k}}\phi^\dagger_{l-\boldsymbol{k}}\right] \\ &+ \frac{U_s}{2}n\cos^2\Phi\sum_{\boldsymbol{k}}\left[\sum_i\phi^\dagger_{i\boldsymbol{k}}\phi_{i\boldsymbol{k}} + \sum_{i\neq j}(\phi^*_i\phi_j\phi^\dagger_{i\boldsymbol{k}}\phi_{j\boldsymbol{k}} + \phi^*_i\phi_j\phi^\dagger_{j\boldsymbol{k}}\phi_{i\boldsymbol{k}}) + \sum_{(ijkl)}\phi^*_i\phi_j\phi^\dagger_{k\boldsymbol{k}}\phi_{l\boldsymbol{k}}\right] \\ &+ \frac{U_s}{2}n\cos^2\Phi\sum_{\boldsymbol{k}}\left[\sum_{ij}\phi^*_i\phi^*_i\phi_{j\boldsymbol{k}}\phi_{j-\boldsymbol{k}} + \sum_{i\neq j}2\phi^*_i\phi^*_j\phi_{i\boldsymbol{k}}\phi_{j-\boldsymbol{k}} + \sum_{(ijkl)}\phi^*_i\phi^*_j\phi_{k\boldsymbol{k}}\phi_{l-\boldsymbol{k}}\right], \end{aligned} \quad \text{(C9)}$$

where $(ijkl)$ denotes all possible permutations of (0,1,2,3). Similarly, the fluctuation for p orbitals is given by

$$\begin{aligned} H^{(2)}_{\mathrm{I},\boldsymbol{p}} &= \frac{U_p}{6}n\sin^4\Phi\sum_{\boldsymbol{k}}\left[\sum_i\left(\frac{16}{9}\phi_i^2 + \frac{11}{9}\sum_j\phi_j^2\right)\phi^\dagger_{i\boldsymbol{k}}\phi^\dagger_{i-\boldsymbol{k}} + \sum_{i\neq j}\frac{22}{9}\phi_i\phi_j\phi^\dagger_{i\boldsymbol{k}}\phi^\dagger_{j-\boldsymbol{k}} + \sum_{(ijkl)}\frac{1}{3}\phi_i\phi_j\phi^\dagger_{k\boldsymbol{k}}\phi^\dagger_{l-\boldsymbol{k}}\right] \\ &+ \frac{2U_p}{3}n\sin^4\Phi\sum_{\boldsymbol{k}}\left[\sum_i\left(\frac{16}{9}|\phi_i|^2 + \frac{11}{9}\right)\phi^\dagger_{i\boldsymbol{k}}\phi_{i\boldsymbol{k}} + \sum_{i\neq j}\frac{11}{9}(\phi^*_i\phi_j + \phi^*_j\phi_i)\phi^\dagger_{i\boldsymbol{k}}\phi_{j\boldsymbol{k}} + \sum_{(ijkl)}\frac{1}{3}\phi^*_i\phi_j\phi^\dagger_{k\boldsymbol{k}}\phi_{l\boldsymbol{k}}\right] \\ &+ \frac{U_p}{6}n\sin^4\Phi\sum_{\boldsymbol{k}}\left[\sum_i\left(\frac{16}{9}\phi_i^{*2} + \frac{11}{9}\sum_j\phi_j^{*2}\right)\phi_{i\boldsymbol{k}}\phi_{i-\boldsymbol{k}} + \sum_{i\neq j}\frac{22}{9}\phi^*_i\phi^*_j\phi_{i\boldsymbol{k}}\phi_{j-\boldsymbol{k}} + \sum_{(ijkl)}\frac{1}{3}\phi^*_i\phi^*_j\phi_{k\boldsymbol{k}}\phi_{l-\boldsymbol{k}}\right]. \end{aligned} \quad \text{(C10)}$$

Collecting the fluctuations discussed above, the Hamiltonian for the quadratic fluctuation is given by

$$H^{(2)}_{\mathrm{QF}} = \mathcal{N}_\mathrm{L}\mathcal{E}^{(2)}(\boldsymbol{\phi}^*,\boldsymbol{\phi}) + H^{(2)}_{\mathrm{TB}} + H^{(2)}_{\mathrm{I},s} + H^{(2)}_{\mathrm{I},p}. \quad \text{(C11)}$$

It is straightforward to construct the effective action by following Ref. [52].

[1] *Introduction to Frustrated Magnetism*, edited by C. Lacroix, P. Mendels, and F. Mila (Springer, Berlin, 2011).

[2] R. Moessner and J. T. Chalker, Properties of a Classical Spin Liquid: The Heisenberg Pyrochlore Antiferromagnet, Phys. Rev. Lett. **80**, 2929 (1998).

[3] B. Canals and C. Lacroix, Quantum spin liquid: The Heisenberg antiferromagnet on the three-dimensional pyrochlore lattice, Phys. Rev. B **61**, 1149 (2000).

[4] S. E. Palmer and J. T. Chalker, Order induced by dipolar interactions in a geometrically frustrated antiferromagnet, Phys. Rev. B **62**, 488 (2000).

[5] J. S. Gardner, M. J. P. Gingras, and J. E. Greedan, Magnetic pyrochlore oxides, Rev. Mod. Phys. **82**, 53 (2010).

[6] A. M. Hallas, J. Gaudet, and B. D. Gaulin, Experimental insights into ground-state selection of quantum XY pyrochlores, Annu. Rev. Condens. Matter Phys. **9**, 105 (2018).

[7] A. M. Hallas, J. Gaudet, N. P. Butch, G. Xu, M. Tachibana, C. R. Wiebe, G. M. Luke, and B. D. Gaulin, Phase Competition in the Palmer-Chalker XY Pyrochlore $Er_2Pt_2O_7$, Phys. Rev. Lett. **119**, 187201 (2017).

[8] S. Petit, E. Lhotel, F. Damay, P. Boutrouille, A. Forget, and D. Colson, Long-Range Order in the Dipolar XY Antiferromagnet $Er_2Sn_2O_7$, Phys. Rev. Lett. **119**, 187202 (2017).

[9] S. Guitteny, S. Petit, E. Lhotel, J. Robert, P. Bonville, A. Forget, and I. Mirebeau, Palmer-Chalker correlations in the XY pyrochlore antiferromagnet $Er_2Sn_2O_7$, Phys. Rev. B **88**, 134408 (2013).

[10] A. S. Wills, M. E. Zhitomirsky, B. Canals, J. P. Sanchez, P. Bonville, P. Dalmas de Réotier, and A. Yaouanc, Magnetic ordering in $Gd_2Sn_2O_7$: The archetypal Heisenberg pyrochlore antiferromagnet, J. Phys.: Condens. Matter **18**, L37 (2006).

[11] I. Bloch, J. Dalibard, and S. Nascimbène, Quantum simulations with ultracold quantum gases, Nat. Phys. **8**, 267 (2012).

[12] I. Bloch, J. Dalibard, and W. Zwerger, Many-body physics with ultracold gases, Rev. Mod. Phys. **80**, 885 (2008).

[13] G. Wirth, M. Ölschläger, and A. Hemmerich, Evidence for orbital superfluidity in the P-band of a bipartite optical square lattice, Nat. Phys. **7**, 147 (2011).

[14] P. Soltan-Panahi, D.-S. Lühmann, J. Struck, P. Windpassinger, and K. Sengstock, Quantum phase transition to unconventional multi-orbital superfluidity in optical lattices, Nat. Phys. **8**, 71 (2012).

[15] M. Ölschläger, T. Kock, G. Wirth, A. Ewerbeck, C. M. Smith, and A. Hemmerich, Interaction-induced chiral $p_x \pm ip_y$ superfluid order of bosons in an optical lattice, New J. Phys. **15**, 083041 (2013).

[16] T. Kock, M. Ölschläger, A. Ewerbeck, W.-M. Huang, L. Mathey, and A. Hemmerich, Observing Chiral Superfluid Order by Matter-Wave Interference, Phys. Rev. Lett. **114**, 115301 (2015).

[17] S. Jin, W. Zhang, X. Guo, X. Chen, X. Zhou, and X. Li, Dynamical emergence of a Potts-nematic superfluid in a hexagonal sp^2 optical lattice, arXiv:1910.11880.

[18] X. Li, E. Zhao, and W. V. Liu, Topological states in a ladder-like optical lattice containing ultracold atoms in higher orbital bands, Nat. Commun. **4**, 1523 (2013).

[19] X. Li, A. Paramekanti, A. Hemmerich, and W. V. Liu, Proposed formation and dynamical signature of a chiral Bose liquid in an optical lattice, Nat. Commun. **5**, 3205 (2014).

[20] B. Liu, X. Li, B. Wu, and W. V. Liu, Chiral superfluidity with p-wave symmetry from an interacting s-wave atomic Fermi gas, Nat. Commun. **5**, 5064 (2014).

[21] H. Chen, X.-J. Liu, and X. C. Xie, Chern Kondo Insulator in an Optical Lattice, Phys. Rev. Lett. **116**, 046401 (2016).

[22] Z.-F. Xu, L. You, A. Hemmerich, and W. V. Liu, π-Flux Dirac Bosons and Topological Edge Excitations in a Bosonic Chiral p-Wave Superfluid, Phys. Rev. Lett. **117**, 085301 (2016).

[23] M. Di Liberto, A. Hemmerich, and C. M. Smith, Topological Varma Superfluid in Optical Lattices, Phys. Rev. Lett. **117**, 163001 (2016).

[24] X. Li and W. V. Liu, Physics of higher orbital bands in optical lattices: A review, Rep. Prog. Phys. **79**, 116401 (2016).

[25] J.-S. Pan, W. V. Liu, and X.-J. Liu, Emergence of the unconventional type-II Nambu-Goldstone modes, arXiv:1910.10072.

[26] J. Villain, R. Bidaux, J.-P. Carton, and R. Conte, Order as an effect of disorder, J. Phys. (Paris) **41**, 1263 (1980).

[27] C. L. Henley, Ordering due to Disorder in a Frustrated Vector Antiferromagnet, Phys. Rev. Lett. **62**, 2056 (1989).

[28] H. T. Diep, *Frustrated Spin Systems*, 2nd ed. (World Scientific, Singapore, 2013).

[29] A. G. Green, G. Conduit, and F. Krüger, Quantum order-by-disorder in strongly correlated metals, Annu. Rev. Condens. Matter Phys. **9**, 59 (2018).

[30] Y. Nambu, Quasi-particles and gauge invariance in the theory of superconductivity, Phys. Rev. **117**, 648 (1960).

[31] J. Goldstone, Field theories with superconductor solutions, Nuovo Cimento **19**, 154 (1961).

[32] K. I. Petsas, A. B. Coates, and G. Grynberg, Crystallography of optical lattices, Phys. Rev. A **50**, 5173 (1994).

[33] O. Toader, T. Y. M. Chan, and S. John, Photonic Band Gap Architectures for Holographic Lithography, Phys. Rev. Lett. **92**, 043905 (2004).

[34] H. Chen and X. C. Xie, Crystalline splitting of d orbitals in two-dimensional regular optical lattices, Phys. Rev. A **98**, 053611 (2018).

[35] C. Chin, R. Grimm, P. Julienne, and E. Tiesinga, Feshbach resonances in ultracold gases, Rev. Mod. Phys. **82**, 1225 (2010).

[36] A. Isacsson and S. M. Girvin, Multiflavor bosonic Hubbard models in the first excited Bloch band of an optical lattice, Phys. Rev. A **72**, 053604 (2005).

[37] W. V. Liu and C. Wu, Atomic matter of nonzero-momentum Bose-Einstein condensation and orbital current order, Phys. Rev. A **74**, 013607 (2006).

[38] P. Nozières, in *Bose-Einstein Condensation*, edited by A. Griffin, D. W. Snoke, and S. Stringari (Cambridge University Press, Cambridge, 1995).

[39] C. J. Pethick and H. Smith, *Bose-Einstein Condensation in Dilute Gases*, 2nd ed. (Cambridge University Press, Cambridge, 2008).

[40] F. Dalfovo, S. Giorgini, L. P. Pitaevskii, and S. Stringari, Theory of Bose-Einstein condensation in trapped gases, Rev. Mod. Phys. **71**, 463 (1999).

[41] M. S. Dresselhaus, G. Dresselhaus, and A. Jorio, *Group Theory: Application to the Physics of Condensed Matter* (Springer, Berlin, 2008).

[42] N. N. Bogolyubov, On the theory of superfluidity, J. Phys. (USSR) **11**, 23 (1947).

[43] A. A. Abrikosov, L. P. Gorkov, and I. E. Dzyaloshinski, *Methods of Quantum Field Theory in Statistical Physics* (Dover, New York, 1963).

[44] A. Kastberg, W. D. Phillips, S. L. Rolston, R. J. C. Spreeuw, and P. S. Jessen, Adiabatic Cooling of Cesium to 700 nK in an Optical Lattice, Phys. Rev. Lett. **74**, 1542 (1995).

[45] M. Greiner, I. Bloch, O. Mandel, T. W. Hänsch, and T. Esslinger, Exploring Phase Coherence in a 2D Lattice of Bose-Einstein Condensates, Phys. Rev. Lett. **87**, 160405 (2001).

[46] P. Pedri, L. Pitaevskii, S. Stringari, C. Fort, S. Burger, F. S. Cataliotti, P. Maddaloni, F. Minardi, and M. Inguscio, Expansion of a Coherent Array of Bose-Einstein Condensates, Phys. Rev. Lett. **87**, 220401 (2001).

[47] M. Köhl, H. Moritz, T. Stöferle, K. Günter, and T. Esslinger, Fermionic Atoms in a Three Dimensional Optical Lattice: Observing Fermi Surfaces, Dynamics, and Interactions, Phys. Rev. Lett. **94**, 080403 (2005).

[48] B. Song, C. He, S. Niu, L. Zhang, Z. Ren, X.-J. Liu, and G.-B. Jo, Observation of nodal-line semimetal with ultracold fermions in an optical lattice, Nat. Phys. **15**, 911 (2019).

[49] P. T. Ernst, S. Götze, J. S. Krauser, K. Pyka, D.-S. Lühmann, D. Pfannkuche, and K. Sengstock, Probing superfluids in optical lattices by momentum-resolved Bragg spectroscopy, Nat. Phys. **6**, 56 (2010).

[50] N. W. Ashcroft and N. D. Mermin, *Solid State Physics*, 2nd ed. (Cengage Learning US, Boston, 1976).

[51] F. Dalfovo and S. Stringari, Bosons in anisotropic traps: Ground state and vortices, Phys. Rev. A **53**, 2477 (1996).

[52] A. Altland and B. D. Simons, *Condensed Matter Field Theory* (Cambridge University Press, Cambridge, 2010).